



Supplement of

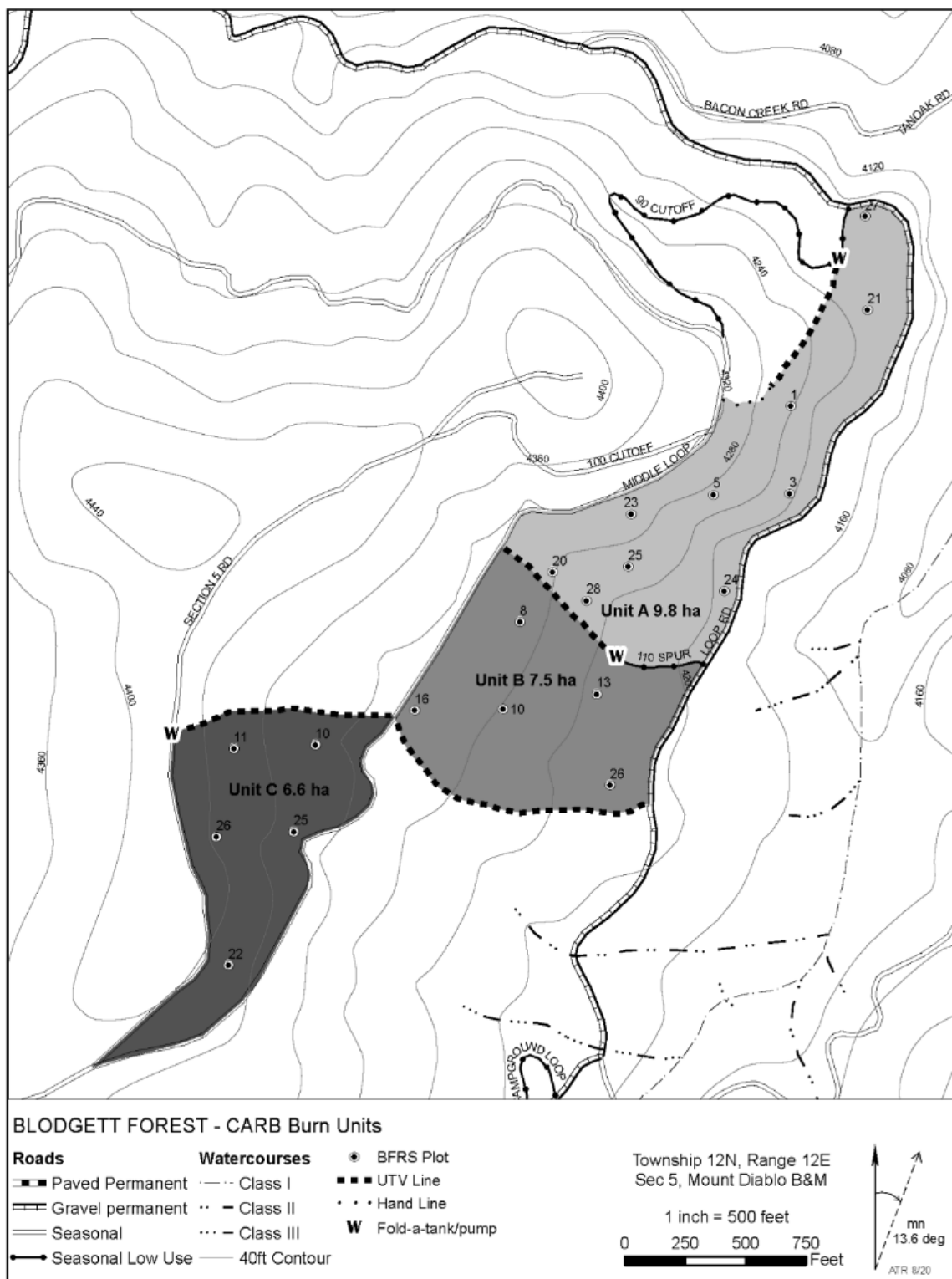
Emission factors and optical properties of black and brown carbon emitted at a mixed-conifer forest prescribed burn

James D. A. Butler et al.

Correspondence to: Thomas W. Kirchstetter (twkirchstetter@lbl.gov)

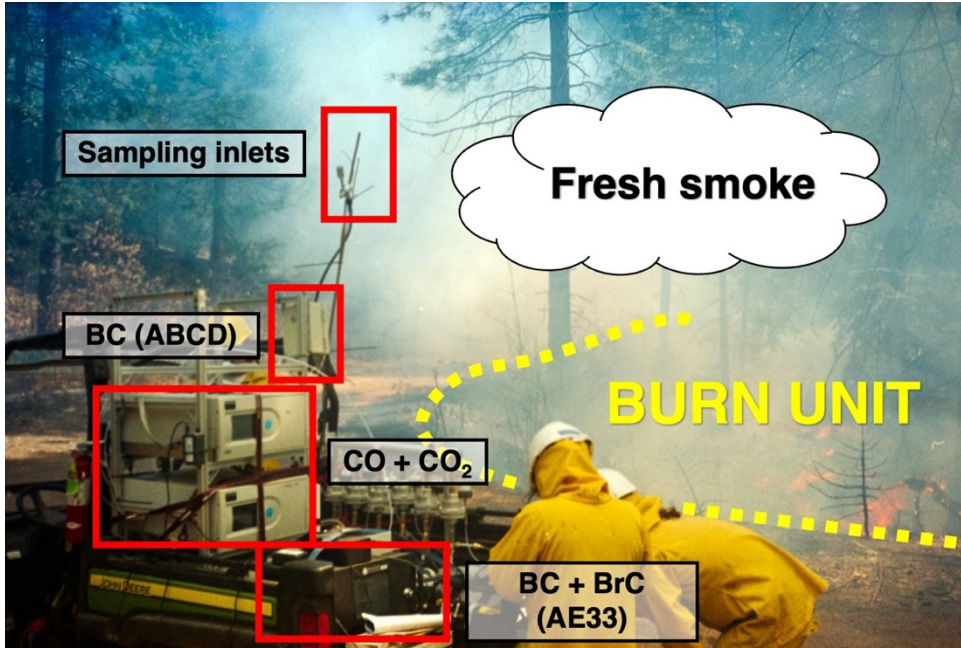
The copyright of individual parts of the supplement might differ from the article licence.

30 **Methods**



31
32 Figure S1: Three units (labeled A, B, C with area noted) treated by prescribed burns at the
33 Blodgett Forest Research Station. Unit A was burned on Days 1 and 2, Unit B on Day 3, Unit C
34 on Day 4.

35



36
37
38
39
40

Figure S2: Ground sampling platform setup on the utility task vehicle with the mounted filter-based photometers and gas analyzers. Sampling inlet shown attached above the roll cage of the UTV.

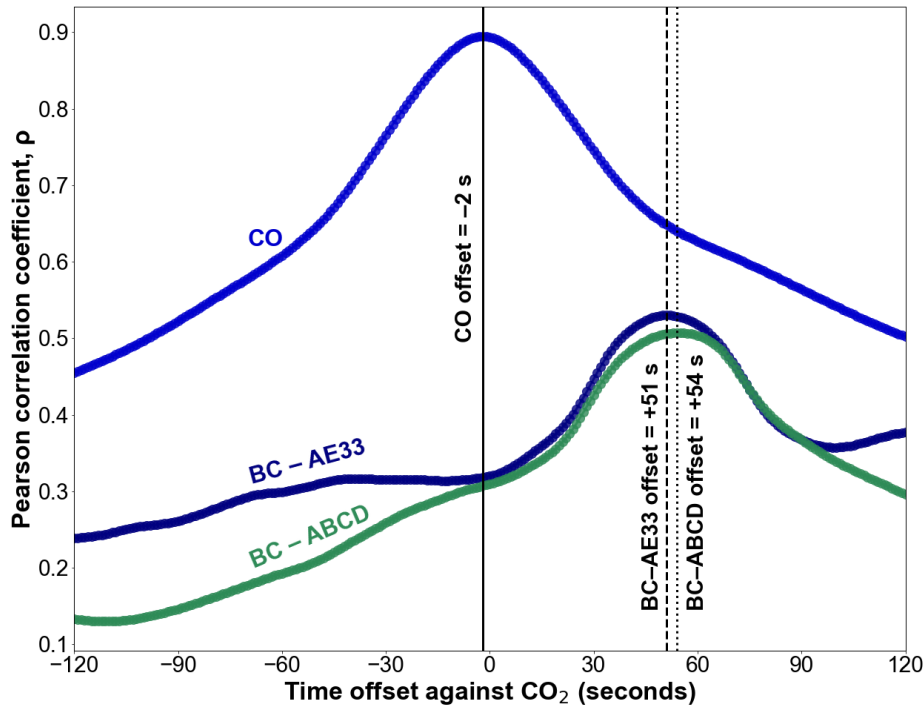
41 **Data Quality Assurance and Control.** Field data were post-processed for quality assurance and
42 quality control before analysis, as described in detail below: (1) datasets from each instrument
43 were time aligned on a 1 Hz time basis; (2) BC measurements were adjusted to account for the
44 filter loading artifact; and (3) timeseries plots of gases and particle concentrations were visually
45 inspected for data quality.

46 **(1) Timestamp Alignment.** To calculate an emission factor (EF) on any time basis, pollutant
47 timeseries and/or peaks needed to be integrated together across analyzers on a synchronized time
48 basis. During field sampling, passing plumes of smoke would cause each analyzer to record a
49 peak in concentration at timestamps that varied by ± 60 seconds. This misalignment of the BrC
50 (AE33), BC (AE33 and ABCD), CO, and CO₂ 1 Hz concentration data on the ground platform
51 was due to variations in analyzer internal clocks and differences in response times of the filter-based
52 photometers and gas analyzers. To remedy this issue and reduce uncertainty in EF
53 integration calculations, a timestamp alignment routine was performed on the AE33 BC dataset,
54 ABCD BC dataset, and CO dataset against the CO₂ dataset.

55 The combustion of fuels in the prescribed burn was the only major source of BC, BrC,
56 CO, and CO₂ during field measurements, so the pollutants measured in the sampled smoke

57 plumes were assumed to be co-emitted and linearly correlated. The Pearson correlation
58 coefficient (ρ) was used to determine the appropriate timestamp offset for each analyzer, as it is a
59 measure of linear correlation between two normally distributed random variables (Schober et al.,
60 2018). These timestamp adjustments were made to the AE33 BC, ABCD BC, and CO datasets.
61 The BrC dataset were not included in the analysis, since its timestamps were identical to the
62 AE33 BC dataset; the AE33 BC timestamp adjustment was applied to the BrC timestamp, too.

63 The alignment routine was written as a *Python* function with *pearsonr* statistical function
64 in the *scipy* library. For each unaligned pollutant dataset, timestamps were artificially offset
65 between -120 to +120 seconds and then ρ was calculated between the unaligned datasets (AE33
66 BC, ABCD BC, & CO) to the CO₂ dataset, as presented in Figure S3. The resulting distribution
67 of calculated ρ for each unaligned pollutant dataset all displayed smooth function within the
68 range of applied timestamp offsets. The timestamp offset for each pollutant was chosen where ρ
69 was maximized. The final adjusted timestamps were offset by -2, +51, and +54 seconds for CO,
70 AE33 BC, and ABCD BC, respectively.



71
72 Figure S3: Pearson correlation coefficient (ρ) of CO, BC AE33, and BC ABCD datasets against
73 CO₂ dataset for a range of timestamp offsets (± 120 seconds). Maximum ρ for each unaligned
74 dataset (marked with a vertical line) corresponds to the chosen timestamp offset of -2, +51, and
75 +54 seconds for the CO, BC-AE33, and BC-ABCD datasets, respectively.

76 (2) **BC Loading Artifact Compensation.** BC datasets were first filtered using the ordinary least
 77 squares (OLS) linear regression calculated from the *statsmodels* library in Python (Josef Perktold
 78 et al., 2024). Following prior work, BC concentrations greater than $100 \mu\text{g m}^{-3}$ and less than the
 79 mean absolute error (MAE) on a 1-minute averaging basis were excluded from the dataset
 80 (Caubel et al., 2019):

$$81 \quad MAE = \frac{\sum_{t_i}^{t_n} |BC(t)|}{n}$$

82 The MAE is a measure of measurement noise and was calculated from background sampling
 83 when prescribed burn smoke was not present (Table S1). On a 1-minute average time-basis, all
 84 coefficients of determination for the OLS regression between the AE33 and ABCD were 0.81–
 85 0.85.

87 Table S1: Mean absolute error (MAE) ($\mu\text{g m}^{-3}$) of aethalometers during background sampling.

Average time-basis	Multiwavelength aethalometer (AE33)	Lower-cost BC sensor (ABCD)
1 second (not averaged)	0.4	2.8
10 second	0.2	0.5
1 minute	0.1	0.2

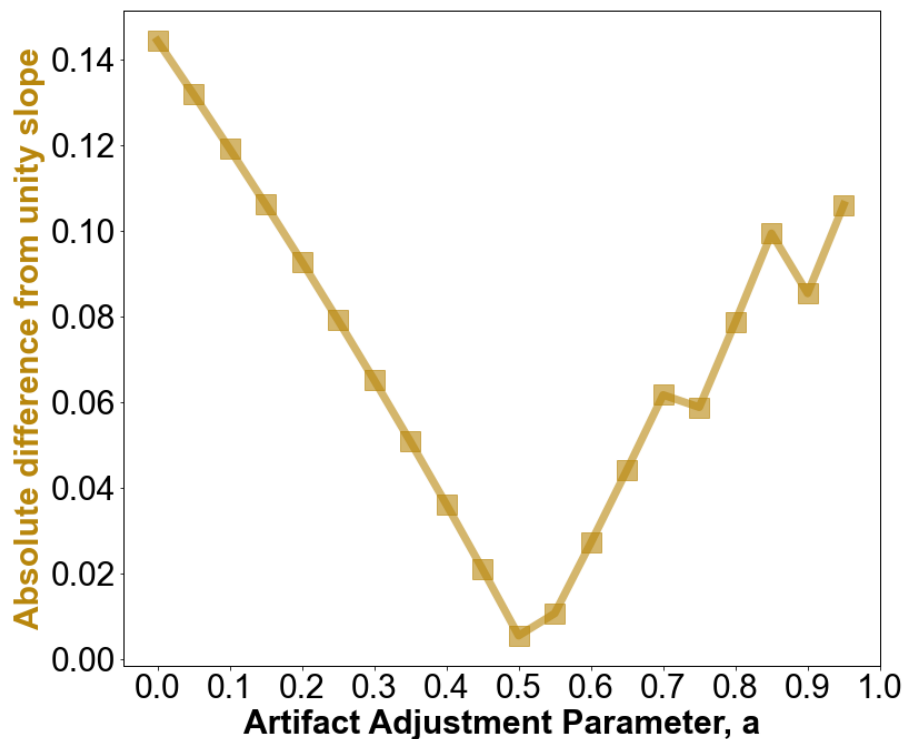
88
 89 Filter-based aerosol absorption photometers become less sensitive to aerosol light
 90 absorption with increasing aerosol deposition, which results in an underestimation of BC
 91 concentration. This is known as the BC loading artifact (Jimenez et al., 2007). The AE33 has a
 92 real-time loading artifact correction algorithm that corrects raw BC concentrations by comparing
 93 the optical attenuation through two filter spots loaded at different flow rates (Drinovec et al.,
 94 2015). Co-location of the ABCD and AE33 provided the basis to apply a source-specific loading
 95 artifact correction to the ABCD BC dataset. For the ABCD BC dataset, data was post-processed
 96 following the method outlined in Caubel et al. (2019), including removing BC concentrations
 97 measured when ATN levels exceeded a value of 100.

98 The ABCD BC dataset was adjusted for its loading artifact using Equation S1, where the
 99 compensation parameter, a , was applied to uncompensated BC concentrations as a function of
 100 measured ATN:

$$101 \quad BC_{ABCD,compensated} = \frac{BC_{ABCD,uncompensated}}{a \cdot \exp\left(-\frac{ATN}{100}\right) + (1-a)} \quad (\text{Equation S1})$$

102 The source-specific value for a was determined by minimizing the difference between 1-minute
103 averaged uncompensated ABCD BC data regressed against averaged auto-compensated AE33
104 BC data (Figure S4). The optimal compensation parameter of $a = 0.5$ resulted in the regression
105 slope closest to unity (Figure S5).

106



107
108 Figure S4: Difference in linear regression slopes from unity of 1-minute averaged ABCD BC
109 dataset, compensated by a , against the AE33 BC dataset.

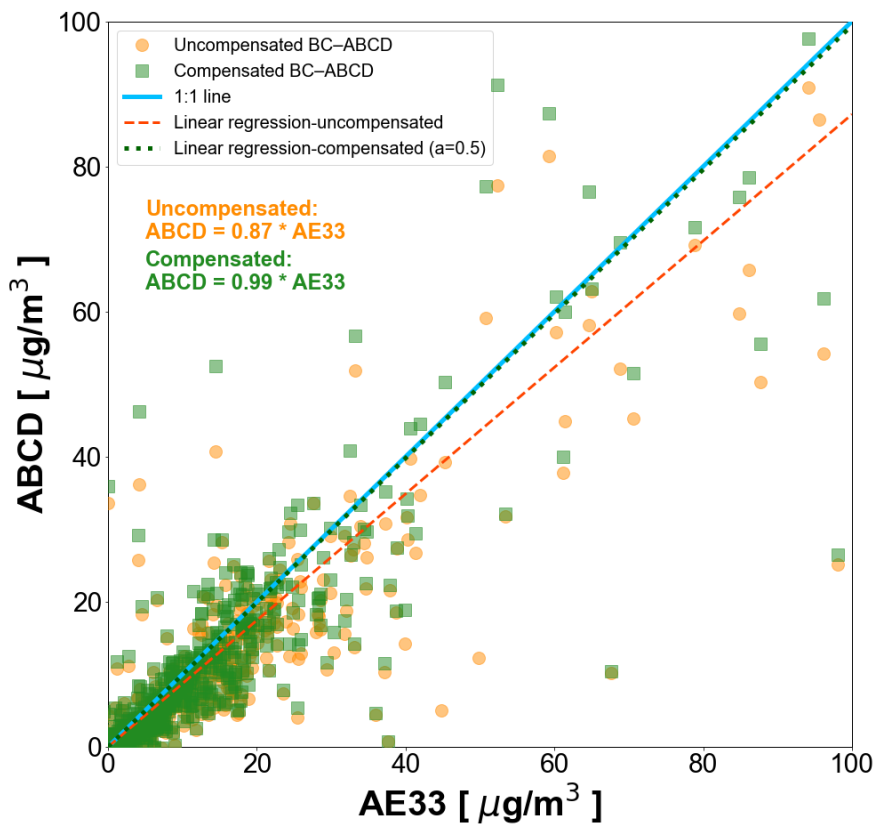
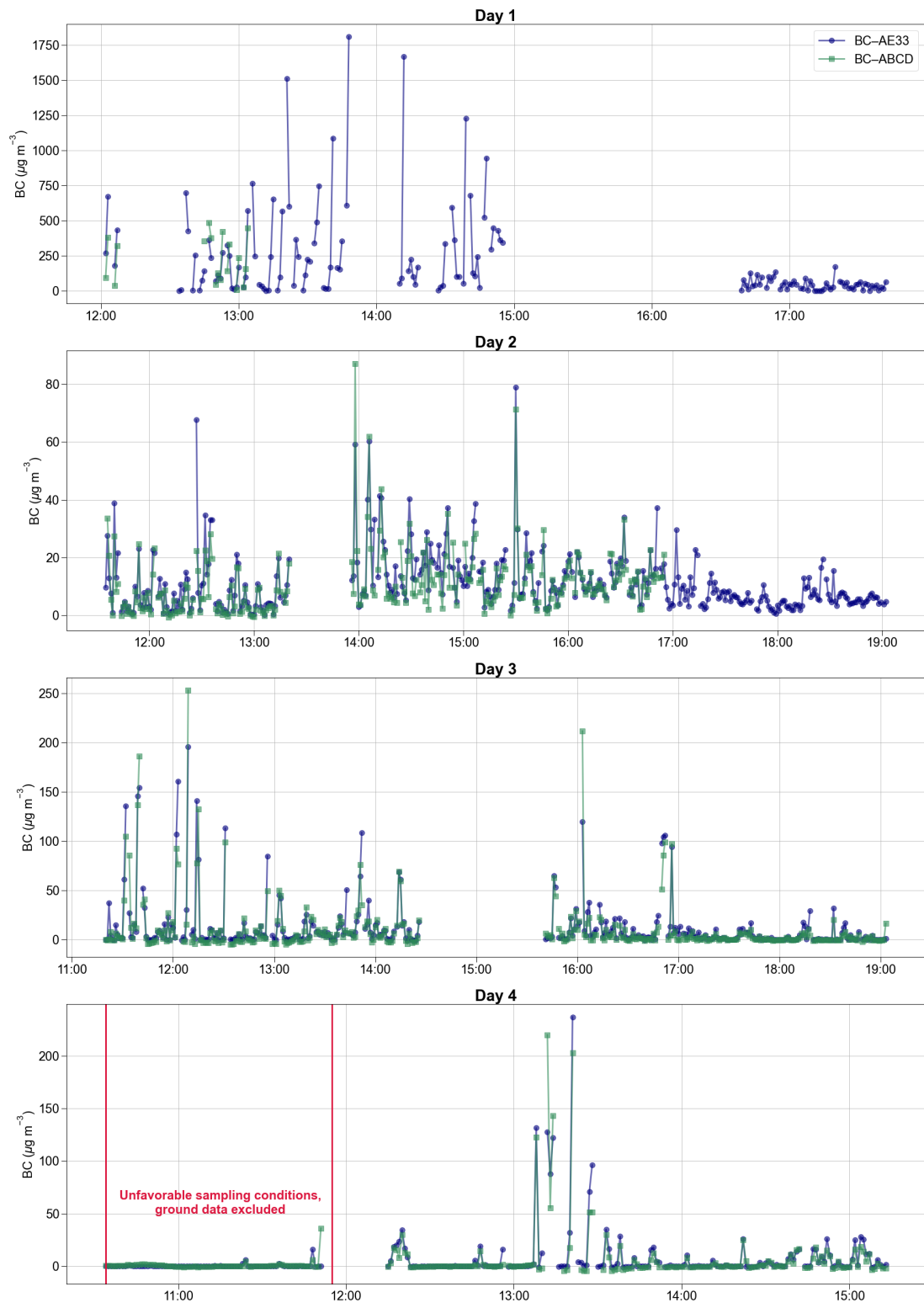


Figure S5: Averaged 1-minute AE33 BC (x-axis) versus ABCD BC (y-axis) before (orange circles) and after (green squares) application of loading artifact compensation. Linear regression slopes displayed, with the compensated slope nearly identical to the unity slope.

(3) Visual Inspection. Timeseries plots were generated for 1-minute AE33 BC and ABCD BC concentrations across the four days of prescribed burns and are presented in Figure S6. Similarly, 1-minute excess CO and CO₂ mixing ratios are presented in Figure S7. For CO, the background concentration was assumed to be zero, as no other sources of incomplete combustion were present at the burn and measured CO concentrations were 1–2 orders of magnitude larger than a trace atmospheric background concentration of around 0.3 ppm. Excess CO₂ was calculated after subtracting the background concentrations listed in Table S2. The CO₂ background concentration was determined daily before the start of the burn for both the ground and aerial sampling platforms. Visual inspection of pollutant timeseries in both Figures S6 and S7 revealed near background concentrations of pollutants during the morning sample session on Day 4, noted in Figures S6 and S7 as having “Unfavorable sampling conditions”. No emission factors or optical properties were computed during this period.



127

128 Figure S6: Timeseries of 1-minute averaged BC concentrations measured by the AE33 and
129 ABCD for each of the four burn days.

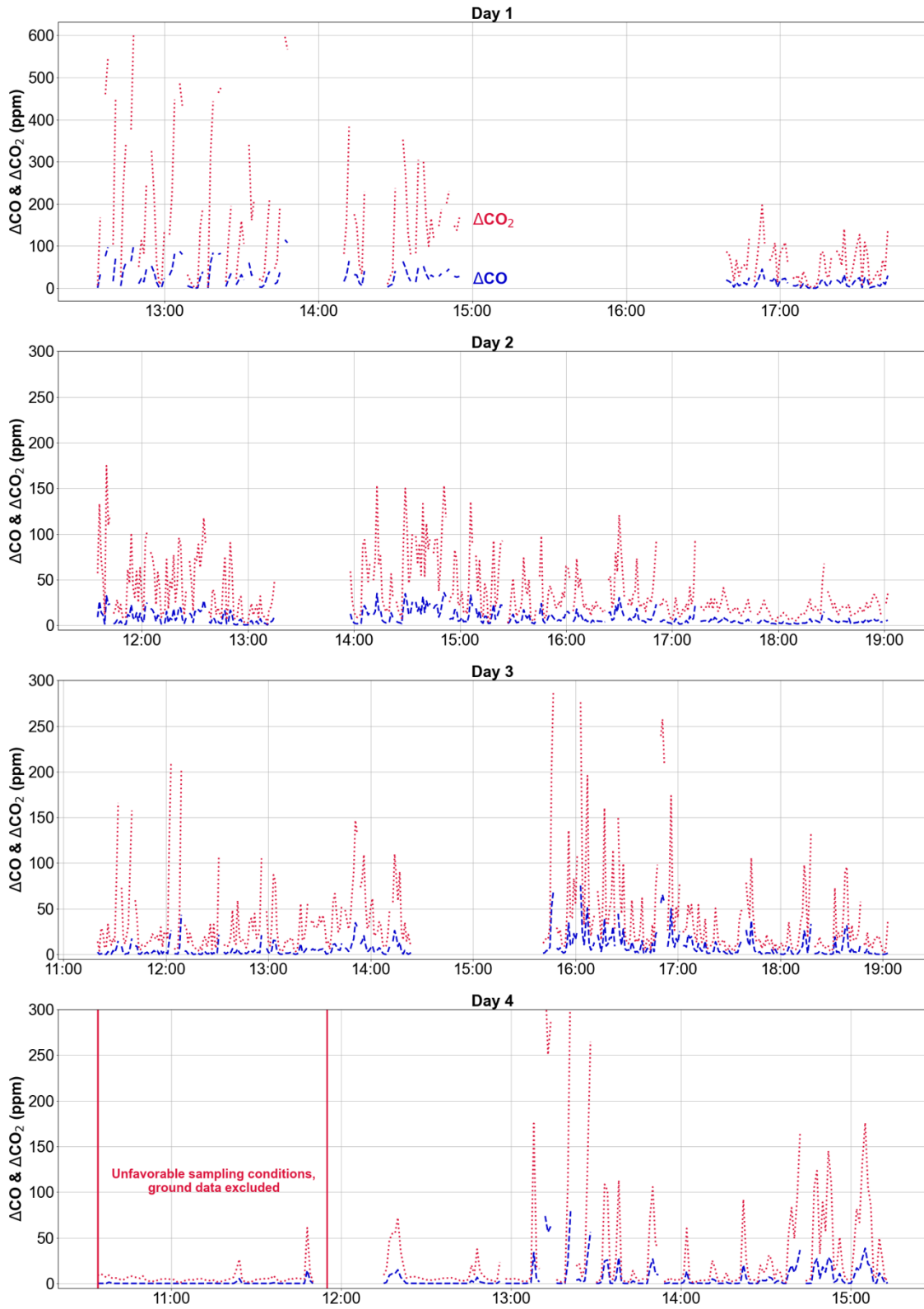


Figure S7: Timeseries of 1-minute averaged excess CO and CO₂, along with modified combustion efficiency (MCE) on the secondary y-axis for each of the four burn days.

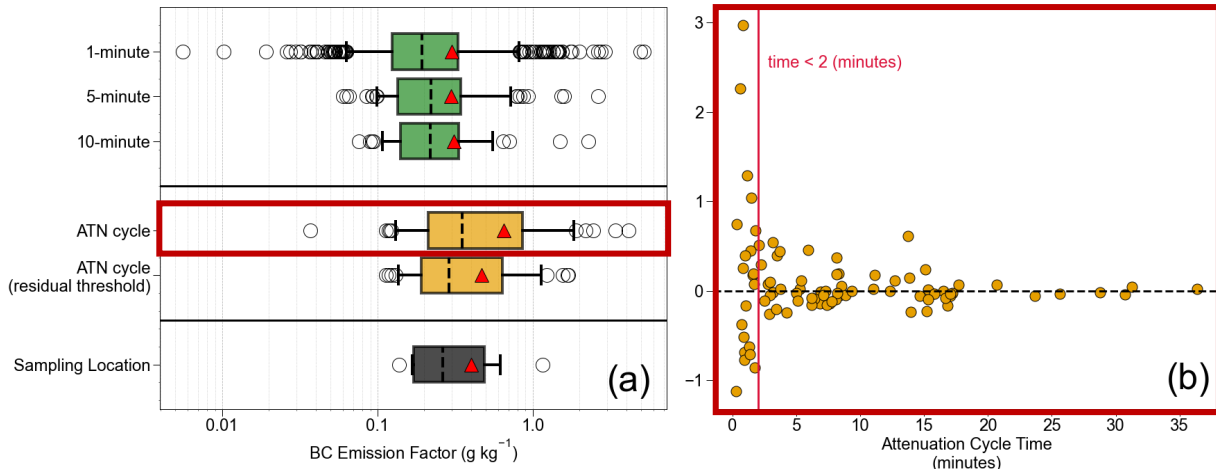
133 Table S2: Background CO₂ concentrations for each day of prescribed burns

Day	Ground CO ₂ [ppm]	Aerial CO ₂ [ppm]
1	409	420
2	410	420
3	404	420
4	402	420

134

135 **Representativeness and Temporal Basis of Emission Factors.** From top to bottom in left panel
 136 of Figure S8, ground BC emission factors were determined using three different approaches: (1)
 137 1-minute, 5-minute, and 10-minute integration windows subsampled from the continuous
 138 dataset, shown in the top panel in green; (2) an ATN cycle basis (i.e., one aethalometer filter tape
 139 advancement), shown in the middle panel in orange; and (3) a sampling location basis, shown in
 140 grey in the bottom panel. The average and median emission factor across the subsample time
 141 bases in the top panel were nearly equal, with an absolute difference of ~ 0.01 and ~ 0.03 g kg⁻¹,
 142 respectively. All three subsample distributions underestimated the sampling location average of
 143 0.40 g kg⁻¹ that is shown in the bottom panel by 0.1 g kg⁻¹. The ATN cycle emission factor
 144 distribution had the greatest average and median values, which exceeded the sampling location
 145 by a factor of 1.6 and 1.3, respectively. Air quality modeling frameworks use a measure of
 146 central tendency, such as an average, as the representative emission factor for a prescribed burn
 147 event in emissions inventories and exposure estimates. By varying the time basis by which
 148 emission factors were calculated, we demonstrate that the average emission factor and shape of
 149 each distribution is sensitive to the chosen integration time basis.

150



151

152 Figure S8: (a) BC emission factor distributions calculated on the ground platform by three
 153 subsampled time bases (1, 5, and 10 minutes – green boxes), the ATN cycle (orange boxes), and
 154 by the sampling location basis (gray box). Boxes represent the interquartile range and tails the 5th
 155 and 95th percentile. The median is provided as the dashed line, the average as a triangle, and
 156 individual values beyond the 5th and 95th percentile whiskers as open circles. Note the
 157 logarithmic scale on the x-axis. (b) BC emission factor residual difference between the ATN
 158 cycle and the sampling location bases plotted against ATN cycle time (minutes) for the ground
 159 platform aethalometer. A residual threshold of 2 minutes is plotted as a vertical line and used in
 160 the lower boxplot in the middle panel of (a).

161

162 The sampling location emission factor distribution ($n = 9$) on the bottom row of the left
 163 panel in Figure S8 is likely the most representative of the prescribed burn. This temporal basis
 164 captured long periods of the event at a fixed location, integrated of all measurement data
 165 minutes, and was consistent with the methodology in previous field studies (Aurell et al., 2021;
 166 Strand et al., 2015). In this work, the minimum sampling location period of 27 minutes was
 167 greater than 95% of ATN cycle times. While this temporal basis may be most representative of
 168 the burn event, it produces the least number of samples and is the least temporally resolved.

169 A greater the number of samples in a field study allows for the investigation of
 170 combustion condition dependence and variability within each combustion regime like the
 171 analyses in Figures 1 and 2. The subsampled emission factors produced the greatest number of
 172 samples and were the most temporally resolved; however, this temporal basis underestimated the
 173 sampling location average because many emission factors were calculated during minimal smoke
 174 capture periods, between passing peaks in concentration, like those shown in Figures S6 and S7.
 175 This effect was pronounced for the most temporally resolved 1-minute emission factors, which

176 were the only distribution to span two orders of magnitude and have values less than 0.03 g kg^{-1}
177 (Figure S8). During minimal smoke capture periods, pollutant concentrations were still elevated,
178 and an emission factor could be calculated. Nevertheless, the bulk of smoke blew away from the
179 ground sampling platform during these minimal smoke capture periods, as shown in Figure S9.
180 Any emission factors computed during these windows were likely not representative of the burn
181 event.

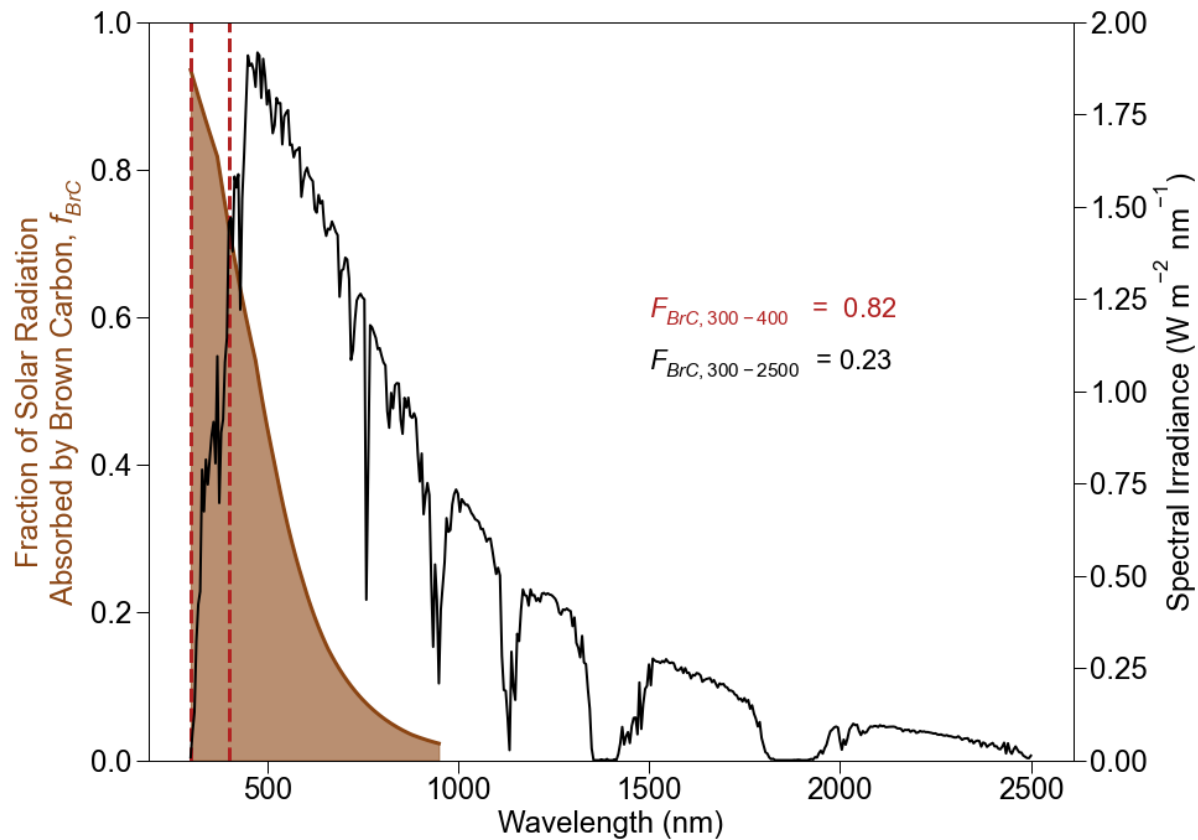
182



183
184 Figure S9: Prescribed burn of Unit C on the morning of Day 4, with ground sampling platform
185 $\sim 10 \text{ m}$ (left) and 20 m (right) directly behind the viewer.
186

187 The temporal basis of the emissions factors calculated on the ATN cycle was variable,
188 with a range of 1–36 minutes. Given the limitations of highly temporally resolved emission
189 factors, residual differences of the ATN cycle and sampling location emission factors are plotted
190 against the ATN cycle time in the right panel of Figure S8. Emission factors calculated during the
191 ATN cycle times less than 2 minutes tended to have highest residual values (i.e., greater than 1 g
192 kg^{-1}), as demarcated by the vertical line in Figure S8. These emission factors were calculated
193 during the highest concentration period of the study, when $\text{BC} > 250 \mu\text{g m}^{-3}$. High BC
194 concentration, and thus a high aerosol loading rate, caused the aethalometer to reach its ATN
195 limit quickly, often before the entire plume of smoke could be measured and before the
196 aethalometer and gas analyzers could return to near-background concentration. Instead, the
197 aethalometer measurements were interrupted by a filter tape advancement and integration of a
198 passing peak in concentration was truncated causing a high residual and unrepresentative
199 emission factor.

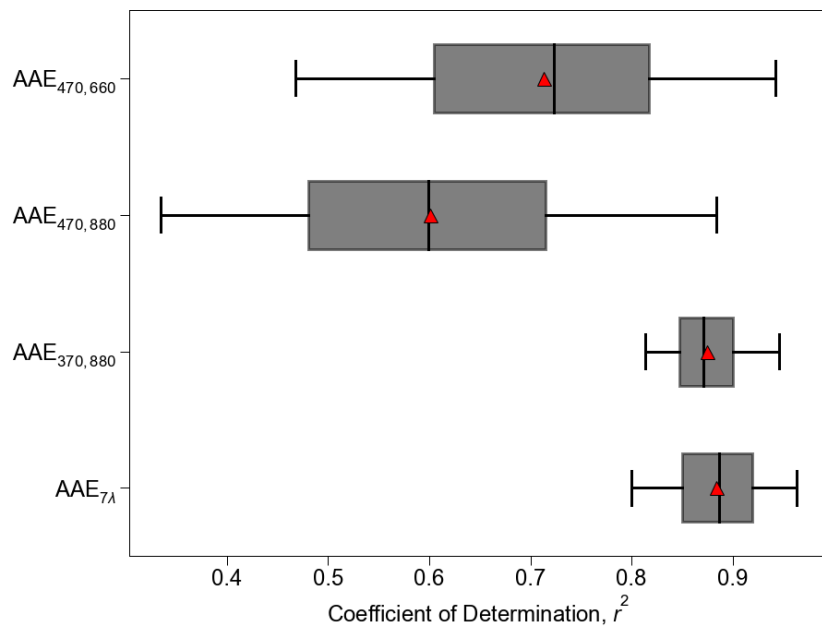
200 When a 2-minute ATN cycle residual threshold was applied, the ATN cycle average BC
201 emission factor was 0.47 g kg^{-1} , which was closest to the sampling location average when
202 compared to the raw ATN cycle and subsample distributions in Figure 4. The residual threshold
203 ATN cycle distribution exhibited the most similar shape to the sampling location distribution, as
204 depicted in the bottom two rows of Figure S8. The residual threshold ATN cycle emission factors
205 also maintained a wider range of MCE values (0.77–0.93) than the sampling location basis
206 (0.79–0.87) that included values in the flaming combustion phase, which supplemented the
207 flaming phase aerial platform emission factors. Retaining field samples on both platforms under
208 flaming and smoldering conditions ensured combustion-phase average emission factors in Figure
209 2 were representative of ground-level and aloft smoke.

210 **Results and Discussion**

211

212 Figure S10: Estimated fraction of solar radiation absorbed by brown carbon (left primary y-axis)
 213 and Air Mass 1 Global Horizontal (AM1GH) spectral irradiance from Levinson et al. (2010)
 214 (right y-axis) plotted as a function of wavelength (x-axis). (Levinson et al., 2010) Integrated
 215 fractions of solar radiation absorbed by brown carbon in the UV region (300–400 nm) and full
 216 spectrum (300–2500 nm) noted.

217



218
219 Figure S11: Coefficient of determination (r^2) for predicted absorption values calculated from
220 power law fit AAEs listed along the y-axis of the figure.

221 **References**

222 Aurell, J., Gullett, B., Holder, A., Kiros, F., Mitchell, W., Watts, A., and Ottmar, R.: Wildland fire
223 emission sampling at Fishlake National Forest, Utah using an unmanned aircraft system, *Atmos.*
224 *Environ.*, 247, 118193, <https://doi.org/10.1016/j.atmosenv.2021.118193>, 2021.

225 Caubel, J. J., Cados, T. E., Preble, C. V., and Kirchstetter, T. W.: A Distributed Network of 100
226 Black Carbon Sensors for 100 Days of Air Quality Monitoring in West Oakland, California,
227 *Environ. Sci. Technol.*, 53, 7564–7573, 2019.

228 Drinovec, L., Močnik, G., Zotter, P., Prévôt, A. S. H., Ruckstuhl, C., Coz, E., Rupakheti, M.,
229 Sciare, J., Müller, T., Wiedensohler, A., and Hansen, A. D. A.: The “dual-spot” Aethalometer: an
230 improved measurement of aerosol black carbon with real-time loading compensation,
231 *Atmospheric Meas. Tech.*, 8, 1965–1979, <https://doi.org/10.5194/amt-8-1965-2015>, 2015.

232 Jimenez, J., Claiborn, C., Larson, T., Gould, T., Kirchstetter, T. W., and Gundel, L.: Loading
233 Effect Correction for Real-Time Aethalometer Measurements of Fresh Diesel Soot, *J. Air Waste*
234 *Manag. Assoc.*, 57, 868–873, <https://doi.org/10.3155/1047-3289.57.7.868>, 2007.

235 Josef Perktold, Skipper Seabold, Kevin Sheppard, ChadFulton, Kerby Shedden, jbrockmendel, j-
236 grana6, Peter Quackenbush, Vincent Arel-Bundock, Wes McKinney, Ian Langmore, Bart Baker,
237 Ralf Gommers, yogabonito, s-scherrer, Yauhen Zhurko, Matthew Brett, Enrico Giampieri, yl565,
238 Jarrod Millman, Paul Hobson, Vincent, Pamphile Roy, Tom Augspurger, tvanzyl, alexbrc, Tyler
239 Hartley, Fernando Perez, Yuji Tamiya, and Yaroslav Halchenko: statsmodels/statsmodels:
240 Release 0.14.2, , <https://doi.org/10.5281/ZENODO.593847>, 2024.

241 Levinson, R., Akbari, H., and Berdahl, P.: Measuring solar reflectance—Part I: Defining a metric
242 that accurately predicts solar heat gain, *Sol. Energy*, 84, 1717–1744,
243 <https://doi.org/10.1016/j.solener.2010.04.018>, 2010.

244 Schober, P., Boer, C., and Schwarte, L. A.: Correlation Coefficients: Appropriate Use and
245 Interpretation, *Anesth. Analg.*, 126, 1763, <https://doi.org/10.1213/ANE.0000000000002864>,
246 2018.

247 Strand, T., Gullett, B., Urbanski, S., O'Neill, S., Potter, B., Aurell, J., Holder, A., Larkin, N.,
248 Moore, M., and Rorig, M.: Grassland and forest understorey biomass emissions from prescribed
249 fires in the south-eastern United States – RxCADRE 2012, *Int. J. Wildland Fire*, 25, 102–113,
250 <https://doi.org/10.1071/WF14166>, 2015.

251